

Upgrade of Thomson Scattering Diagnostic on HL-2A

Wenping Guo¹, Yuan Huang^{1,*}, Chunhua Liu¹, Zhen Feng¹, Zhipei Hou¹, Wenyan Zhai¹, Hisamichi Funaba², Ichihiro Yamada², Yonggao Li¹ and Zhongbin Shi¹

¹ Southwestern Institute of Physics, Chengdu 610041, China

² National Institute for Fusion Science, Toki 509-5292, Japan

* Correspondence: yhuang@swip.ac.cn

Abstract: The Thomson scattering diagnostic of the HL-2A tokamak device was upgraded to improve its multi-point diagnostic capability, including new collection optics, fibers bundles, and data analysis code. The small old collection lens was replaced by a six-piece lens with a Cooke optical design. The aperture of its first standard sphere face is 310.125 mm, which successfully increases the amount of collected scattering light by about three times. The new collection optic module allows for up to twenty-six spatial points. A kind of Y-type fiber bundle has also been used to ensure that the fiber end-face matches the image of the laser beam exactly. Additionally, the new data analysis code can provide preview results in seconds. Finally, the multi-point T_e diagnostic ability has been significantly improved.

Keywords: Thomson scattering; tokamak; collection optics; fiber bundles



Citation: Guo, W.; Huang, Y.; Liu, C.; Feng, Z.; Hou, Z.; Zhai, W.; Funaba, H.; Yamada, I.; Li, Y.; Shi, Z. Upgrade of Thomson Scattering Diagnostic on HL-2A. *Instruments* **2023**, *7*, 12. <https://doi.org/10.3390/instruments7010012>

Academic Editors: Antonio Ereditato and Pasquale Arpaia

Received: 22 December 2022

Revised: 27 February 2023

Accepted: 2 March 2023

Published: 6 March 2023



Copyright: © 2023 by the authors. Licensee MDPI, Basel, Switzerland. This article is an open access article distributed under the terms and conditions of the Creative Commons Attribution (CC BY) license (<https://creativecommons.org/licenses/by/4.0/>).

1. Introduction

Thomson scattering (TS) is an important system for diagnosing electron temperature and density, not only in tokamaks [1–12] but also in stellarators [13], amongst others [14]. The hardware of a typical TS system mainly consists of a high-energy-pulsed laser, collection optics, fiber bundles, polychromators, a high-speed acquisition system, and a control system. The electron temperature and density are obtained by gaining the scattering spectrum from plasma and analyzing it with the incoherent Thomson scattering theory. However, Thomson scattering systems have difficulty obtaining scattered signals because of a sensitive dependence on the alignment between the laser path and the field of view (FOV) of the collection optics, the collection volume size, and the total optical transmission. These are the keys to the final Signal-to-Noise Ratio (SNR). They directly determine the strength of the light that arrives at detectors in a polychromator.

The HL-2A core TS system has a Nd: YAG (yttrium aluminum garnet) laser, which works at 1064 nm(wavelength)/30 Hz (repetition frequency)/3.5 J (energy)/10 ns (pulse width). However, the original collection's optical lens of HL-2A TS was too small to capture enough scattering light from low-parameter plasma (1 keV and $1 \times 10^{19} \text{ m}^{-3}$). Its first-face aperture was only 152.04 mm. This resulted in a small collection volume size and few photons passing it and reaching the polychromator detector. Under this condition, only the very core TS measurement points could collect signals with available SNR. It was thus impossible to reach the required spatial resolution by using the old TS system on HL-2A [2,15,16]. The collection optics are thus redesigned to have a bigger light-input aperture. The aims of the upgrade are to increase the amount of collected scattering light and try to obtain the profile information of the plasma, especially the equilibrium profile, which is the basis of the physics analysis.

The concept of the optical collection module is similar to the one of common camera lenses. Special attention was given to the design of the high light throughput. Therefore, lenses with bigger apertures and new fiber bundles (NA = 0.37) have been systematically designed. The new collection optics can increase the light throughput over three times and

provide a spatial resolution with twenty-six fiber slots. In addition, A Y-type design of the fiber bundle has also been used to help us align the fiber end-face to the image of the laser beam [17,18]. Finally, an efficient data-processing code is adopted to quickly preview T_e after every experimental shoot.

2. Collection Lens

A 350 mm diameter window of silica glass, 1120 mm away from the laser path, has limited the largest FOV for the collection optics. To maximize the collection surface as much as possible and combine it with the newly built heavy ion beam probe (HIBP) system, the optical axis of the new lens is inclined at 9 degrees to the horizontal plane, as Figure 1. shows. As shown in the layout in Figure 1, the lens is based on a Cooke achromatic design and is composed of six single pieces [19]. The height of the corresponding FOV is -500 mm to 300 mm from the midplane. Because the lens module is installed with a 9° slant angle to the midplane ($Z = 0$), the intersection point of the optical axis and laser has a value of $Z = -100$ mm. The FOV can thus cover the plasma downward to the down separatrix of HL-2A, and the length of the line along the laser-beam trajectory from the top to the bottom is ~ 800 mm.

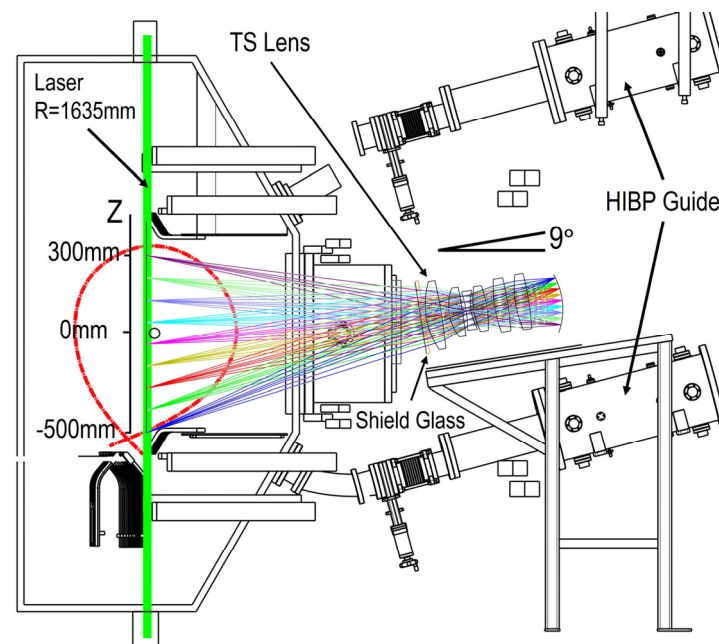


Figure 1. View of the new TS collection's lens layout and nearby HIBP system. Here, the red curve is the plasma separatrix.

The design of the lens has also taken into consideration the cost of material fabrication. Three kinds of accessible commercial glass (BK7, H-K9L, and SF6) are chosen. Furthermore, the type of all the surfaces is set as a standard sphere face. The diameter of the first face of the lens is designed to be 310.125 mm, with a collection area that is ~ 4.1 times that of the old lens. The image surface is also a sphere face with a radius of 305.855 mm, which is simple to manufacture. Finally, the joint weight of the product of collection lenses and the assembled shell is ~ 200 kg. The detailed parameters of lenses, such as the curvature, thickness, distance between lenses, refractive index, and mechanical dimensions, are listed in Table 1.

Table 1. The parameters of the new lens design.

Surface	Radius (mm)	Thickness (mm)	Glass	Clear Semi-Dia (mm)
1	Infinity	15.000	H-K9L	165.564
2	Infinity	10.000		163.668
3	369.720	70.000	BK7	155.125
4	−2064.825	35.000		146.487
5	234.155	60.000	BK7	111.789
6	−3000.000	16.900		96.211
STOP	−533.310	22.000	SF6	85.000
8	241.000	12.872		88.011
9	341.125	60.000	BK7	93.612
10	−507.900	35.000		102.123
11	576.290	60.000	BK7	116.281
12	−1479.100	35.000		119.973
13	479.020	60.000	BK7	124.904
14	−1277.800	149.396		123.590
IMAGE	−305.855			

For the experimental configuration, the effective focal length in the image space is 324.219 mm, the working F number is 2.0473, and the paraxial magnification of the lens module is −0.279. The max image space NA is 0.2431. If there is no anti-reflection (AR) coating on the faces, the total transmission of the lens module and silica window is about 46%. Every surface is thus AR-coated for a wavelength of 500–1100 nm, which is expected to increase the total transmission to over 60%. The lens supplies a well-focused image, as shown in the root mean square (RMS) spot radius and spot diagram in Figure 2. For wavelengths of 700 nm, 800 nm, 900 nm, and 1000 nm, the RMS radii are all smaller than 170 μm. Here, the RMS spot radius gives a rough idea of the spread of the rays; the distance between each ray and the reference point is squared and averaged over all the rays. It depends on every ray and thus encloses most of the energy. The spot diagrams of the corresponding TS spatial points are also small enough both on and off the axis. As the vignetting diagram shows in Figure 3, the collection’s optic lens can also present a vignetting under 10% at 300 mm. In other words, most images of the spatial points in the FOV are clear enough and lose little energy.

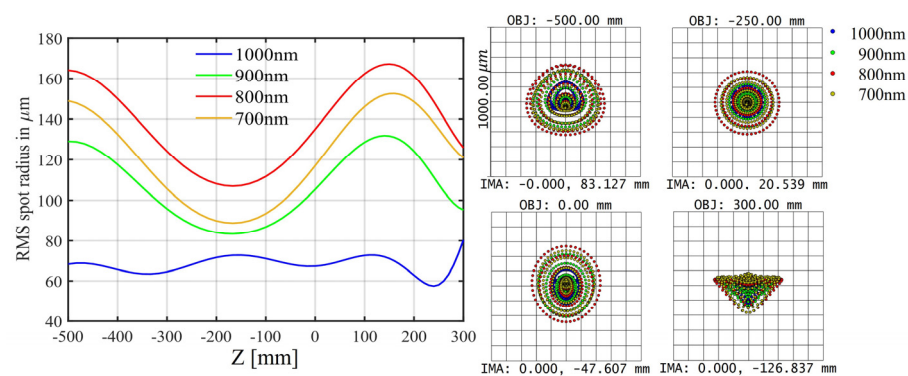


Figure 2. The RMS spot radius of images (IMA) versus Z value along the laser beam, and the spot diagram of the collection module for four objects (OBJ, i.e., TS measurement points).

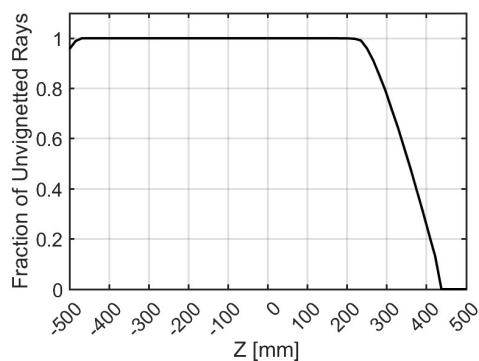


Figure 3. Vignetting diagram of the lens module.

When other parts of the TS system remain the same, the increase of the input solid angle is the key to higher SNR. As a comparison, the old lens was much smaller. The maximum aperture of the old lens was only 152.036 mm. Although the image quality was a little better, the FOV and the amount of light input were much smaller. The FOV of the old one could not cover an area other than ± 400 mm. Correspondingly, a comparison of the collection solid angle versus FOV can be found in Figure 4. The solid angle of the old one was too small to capture enough photons for high SNR signals. Additionally, the new lens can supply about a threefold larger collection solid angle.

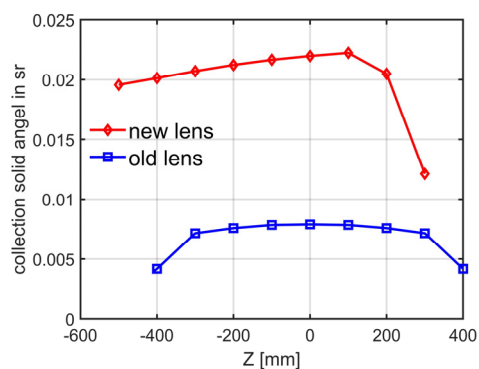


Figure 4. The collection solid angle in sr. versus Z fields in mm of the new and old lenses, respectively.

3. Fiber Bundles

To transmit as much light as possible from the laser-beam image to the polychromator, a kind of low hydroxyl quartz fiber was used. It has a uniform and high transmission ($>99\%/m$) over a wavelength ranging from 600 nm to 1100 nm. Its NA equals 0.37, and it can thus have the margin to cover the image solid angle of the optical lens. It is also cheaper and just right for the input design of the polychromator. Its core diameter is $200 \pm 3 \mu\text{m}$, and the total diameter including cladding is $230 \pm 10 \mu\text{m}$.

To capture the light at the image face, a fiber-bundle clamping apparatus, which holds fiber bundles, is installed on a goniometric rotation stage that stands on a linear stage. The two operational dimensions are both perpendicular to the light axis to make an intensive movement. The clamping apparatus consists of two curved aluminum parts with a radius of 305.855 mm, forming a column of slots between them. The fiber bundles can be inserted into these slots, and the end-face can then locate exactly where the laser-beam image is. Because of gaps for inserting fiber bundles, the module can hold 26 fiber bundles of two types, as shown by the design and pictures in Figure 5. The length of the two types of bundles is 23 m in both cases. The two end-faces of the fiber bundles are also AR-coated to decrease face reflection. However, a small proportion of fibers were broken during production and installation.

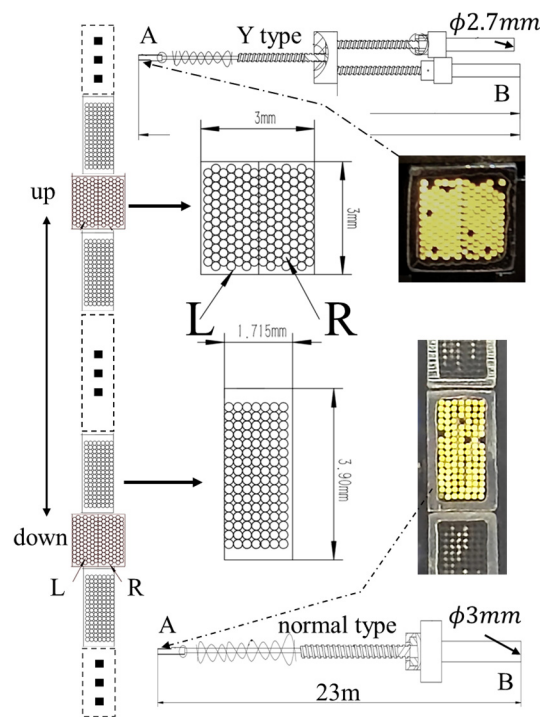


Figure 5. Arrangement design of the slots for fiber bundles, A\B-side design of the fiber bundles, and their pictures. Side A is defined as the input face located at the image face, and side B is the output side inserted into the polychromator. “L” is left, and “R” is right.

The first type is the Y-type. This type of bundle is divided into two channels according to the left and right sides of the image [17,18]. At side A (defined as the input side), ~160 fibers are contained in a square face in a side of 3 mm. At side B (defined as the output side), the fibers from the left and right sides of side A are reshaped into a circular interface to match the energy monitor. Each channel of side B has ~80 fibers. The energy monitor thus has two channels. To satisfy the response-time requirement, it uses the same avalanche photodiode detectors (APD) as other polychromators but without channel filters. However, a narrow-band notch filter for 1064 nm remains in order to suppress stray light. Therefore, we can compare the strength of scattering light from the two sides by using the two-channel energy monitor. When the fiber end-face is exactly aligned with the laser-beam image, the light intensity at the two halves should be equal. Two bundles of this type are set near the up and down edges of the clamping apparatus to ensure that the curved fiber input face is parallel to the image.

The other type of fiber bundle, which is designed for actual TS measurements, holds 112 fibers. Its side A is arranged in a rectangle measuring 1.715 mm × 3.9 mm to collect scattering light along the image face of the laser beam. A bundle corresponds to approximately 1.5~2 cm of plasma along the laser beam. It must also be noted that the laser within the FOV should be focused and thinner than 7 mm. Its image can then be completely covered by the bundle end-face because the magnification of the lens module is ~0.279. At side B of the polychromator entrance, the bundle head is cylindrical with a 3 mm diameter.

4. Data Preview Code

The upgrades of the collection optics can increase the detected scattering signal from ~60 mV up to ~200 mV under the condition of the same environment temperature, same ADP voltage configuration, and similar plasma parameters (~ 1 keV, $3 \times 10^{19} \text{ m}^{-3}$). Figure 6 shows the original signals of a 5-channel polychromator for the core point. The legends in panel (a) correspond to the channel responses of the polychromator shown in panel (b). Clear signals can be observed on all five spectral channels. The maximum SNR is more than 40 times on ch3 and over 10 times on ch5. The corresponding plasma current and

midplane line average electron density are shown in Figure 7a,b. It should be noted that the stray light has been completely cut off by a notch filter, located inside the polychromator after its shaping lenses in the entrance.

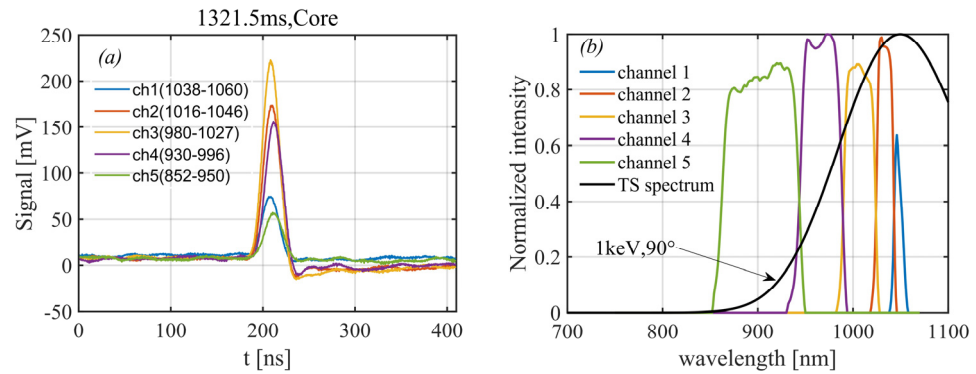


Figure 6. (a) The waveforms of the final signals of five channels for the core point. (b) The relative response versus wavelength of the five channels of the corresponding polychromator for the core point; and the normalized theoretical TS spectrum of 1 keV at a scatter angle of 90°.

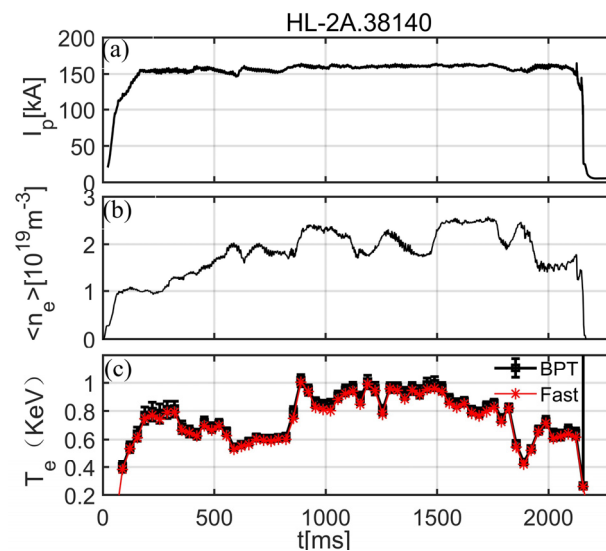


Figure 7. (a,b) Time trace of the plasma current and midplane line average electron density by Far Infrared Ray interference system (FIR). (c) Time evolution of the core plasma temperature obtained by two fitting programs. “BPT” is the program based on the Bayesian probability inference method in [15], and “Fast” is the code used here for the T_e preview.

Better SNR also makes data analyses easier. A simple code is adopted to provide a fast preview of the time evolution of the core T_e . It includes two main functions. The first one is to extract the pure scattering signal intensity for a channel from the outputted pulse waveforms. The waveforms are digitized by the CAEN switched capacitor digitizer V1742 at 2.5 GSa/s. Each segment includes 1025 12-bit data and corresponds to a ~400 ns duration after the trigger from the laser light. However, because the photons arrive at APD at different times and the channels are mutually independent after APD output, there are a few differences between these waveforms. The value of $|s_{peak} - \langle s_{noise} \rangle|$ of a pulse waveform is then considered as a pure scattering signal intensity. Here, $\langle s_{noise} \rangle$ is the average value of the data outside of the central scattering pulse in the waveform. Generally, the noise amplitude is 5~10 mV for most channels.

The second function of the code is to quickly and accurately match the scattering spectrum with the calibration data to obtain T_e . The pure response signals of five channels are first standardized to standard scores:

$$s'_i = \frac{s_i - \bar{s}}{\sigma_{(s_i)}} \quad (1)$$

Here, s_i is the pure signal strength of a channel, and subscript i is the number of channels that have enough SNR and can thus be used for calculation. $\langle \bar{s} \rangle$ is their average value, and $\sigma_{(s_i)}$ is their standard deviation. s'_i is the standard score, which shows the relative value of the signal. This standardization can more effectively drop the effect of the vertical dimension (different amplitude of the scattering signals and calibration data). The calibration data of the channel response dependent on T_e is also transformed into the standard score. Then, T_e is obtained by scanning the lowest Minkowski distance:

$$L(T_e) = \left(\sum_{i=1}^n |s'_i - c'_i(T_e)|^p \right)^{\frac{1}{p}} \quad (2)$$

Here, n is the total number of channels used for data fitting. $c'_i(T_e)$ is the standard score of the calibration data in function of T_e . $p = 1, 2, \dots, \infty$ is the power series. When $p = 1$, $L(T_e)$ is the Manhattan distance. When $p = 2$, $L(T_e)$ is the Euclidean distance, and the method of Equation (2) is exactly the least square method of data fitting. $p = 2$ is also a general configuration. The above algorithm is also one of the basic methods used for voiceprint recognition.

The error of the data, including photon statistical noise, electronic noise, and plasma background light noise, is considered an uncertain background fluctuation under noise amplitude. The possible T_e values can thus be obtained by fitting the modified channel signal, which equals $s_i + s_{i,r}$. Here, $s_{i,r}$ is a random value whose absolute value is smaller than the maximum noise $(\bar{s}_{noise})_{max}$. Moreover, the Bayesian probability inference method was also tested and evaluated [15]. As the results show in Figure 7c, the fast preview code can supply results (without an error bar) that are very close to the complex Bayesian algorithms. However, the fast preview code only takes seconds, while BPT (“BP” is Bayesian Probability, and “T” is the mark for “Test”) requires tens of minutes by the same software on the same PC. The error bars for the BPT are also small due to a high SNR.

5. Results

The multi-point plasma temperature profile can now be measured by the upgraded TS system. As shown in the example in Figure 8, when the plasma current was ~160 kA and the core electron density was $\sim 3 \times 10^{19} \text{ m}^{-3}$, twelve points were successfully measured. The overall temperature profile obviously rose when the Electron Cyclotron Resonance Heating (ECRH), Low Hybrid (LH) waves, and Neutral Beam Injector (NBI) were injected to successfully drive the H-mode, i.e., the Edge-Localized Mode (ELM) happened. The increase of the electron temperature of the outer region ($Z/a = \sim 0.8$) predicted a significant increase in the edge temperature gradient, which was in exact agreement with the profile characteristics during ELMs.

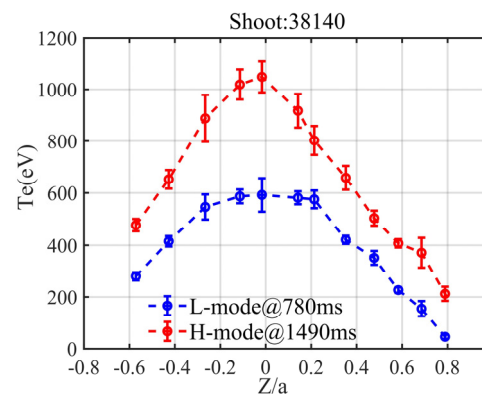


Figure 8. The temperature profiles measured by the upgraded HL-2A TS system at two moments of the L-mode and H-mode, respectively. Z is the height to the midplane of the measurement point, and $a = 400$ mm is the minor radius.

There were eighteen polychromators and two aiming monitors assembled after this upgrade. However, only 12 TS measurement points that were closer to the core could capture signals that were sufficiently strong. The SNR of some channels of the other six polychromators for the edge region was too low to be calculated. The first reason for this was that T_e , n_e at the edge was much lower, but the filters of these polychromators were not yet completely compatible with the characteristics of the TS scattering spectrum of the edge plasma. The second reason was that the slit for the beam path of the original divertor plate of HL-2A was too narrow (~ 10 mm). It caused a strong stray light that significantly affected the signals, especially on the channel for low T_e . Therefore, the available spatial points were still not sufficient to satisfy a fine physics research. An upgrade of the polychromator for edge plasma and partial modification of the divertor plate are in the works.

6. Conclusions

To improve the multi-point diagnostic capability of the HL-2A TS system, a new collection optic module has been designed and produced to increase the final SNR. The new lens is a six-piece Cooke type, whose collection solid angle is about three times as high as the old one. The clamping apparatus can hold 26 fiber bundles for spatial resolution. Experimental data from the new collection module shows that SNR has accordingly increased about threefold, and 12 points have been diagnosed successfully. T_e could also be rapidly previewed by the new calculation code, whose results are in strong agreement with the complex algorithm based on the Bayesian probability inference method. The system has been prepared so as to provide more and better data in the coming experimental campaigns once the divertor plate has been modified and more polychromators have been delivered.

Author Contributions: TS team: W.G., Y.H., C.L., Z.F., Z.H. and W.Z.; FIR data: Y.L.; review: H.F., I.Y. and Z.S.; All authors have read and agreed to the published version of the manuscript.

Funding: This work was supported by the project of the China National key research and development plan: No. 2018YEF0301102, the Natural Science Foundation of China (Grant No. 11775072), and the University and Institute Cooperation Project of Sichuan Province (Grant Nos. 2020YFSY0046 and 2021YFSY0044).

Data Availability Statement: The raw data are available on request from the corresponding authors.

Acknowledgments: The authors would like to thank the HL-2A's administration team and the engineering team for their support and help in the experiment.

Conflicts of Interest: The authors declare no conflict of interest.

References

1. Narihara, K.; Yamada, I.; Hayashi, H.; Yamauchi, K. Design and performance of the Thomson scattering diagnostic on LHD. *Rev. Sci. Instrum.* **2001**, *72*, 1122–1125. [[CrossRef](#)]
2. Huang, Y.; Zhang, P.; Feng, Z.; Liu, C.H.; Shi, P.L.; Ding, X.T.; Liu, Y. The development of Thomson scattering system on HL-2A tokamak. *Rev. Sci. Instrum.* **2007**, *78*, 113501. [[CrossRef](#)] [[PubMed](#)]
3. Li, Y.; Baonian, W.; Junyu, Z.; Qingsheng, H.; Yanqing, J.; Xiaoqi, X.; Xiaofeng, H.; Qing, Z. Design of Thomson Scattering Diagnostic System on EAST. *Plasma Sci. Technol.* **2010**, *12*, 284–288. [[CrossRef](#)]
4. Ponce-Marquez, D.M.; Bray, B.D.; Deterly, T.M.; Liu, C.; Eldon, D. Thomson scattering diagnostic upgrade on DIII-D. *Rev. Sci. Instrum.* **2010**, *81*, 10. [[CrossRef](#)] [[PubMed](#)]
5. Qing, Z.; Junyu, Z.; Li, Y.; Qingsheng, H.; Yanqing, J.; Tao, Z.; Xiaoqi, X.; Bhatti, S.H.; Xiang, G. Development of a Thomson Scattering Diagnostic System on EAST. *Plasma Sci. Technol.* **2010**, *12*, 144–148. [[CrossRef](#)]
6. Kurzan, B.; Murmann, H.D. Edge and core Thomson scattering systems and their calibration on the ASDEX Upgrade tokamak. *Rev. Sci. Instrum.* **2011**, *82*, 103501. [[CrossRef](#)] [[PubMed](#)]
7. Tojo, H.; Pasqualotto, R.; Fassina, A.; Giudicotti, L.; Sasao, H.; Homma, H.; Oyama, N. Design of JT-60SA core Thomson scattering diagnostic system. *Rev. Sci. Instrum.* **2021**, *92*, 043556. [[CrossRef](#)] [[PubMed](#)]
8. Li, H.Y.; Li, S.J.; Xie, Q.F.; Liu, J.H.; Bai, R.H.; Tao, R.Y.; Lun, X.C.; Li, N.; Bo, X.K.; Liu, C.Q.; et al. Thomson scattering diagnostic system for the XuanLong-50 experiment. *Rev. Sci. Instrum.* **2022**, *93*, 053504. [[CrossRef](#)] [[PubMed](#)]
9. Scannell, R.; Walsh, M.J.; Carolan, P.G.; Conway, N.J.; Darke, A.C.; Dunstan, M.R.; Van Hare, D.R.; Prunty, S.L. Enhanced edge Thomson scattering on MAST. *Rev. Sci. Instrum.* **2006**, *77*, 10E510. [[CrossRef](#)]
10. Scannell, R.; Walsh, M.J.; Carolan, P.G.; Darke, A.C.; Dunstan, M.R.; Huxford, R.B.; McArdle, G.; Morgan, D.; Naylor, G.; O’Gorman, T.; et al. Design of a new Nd:YAG Thomson scattering system for MAST. *Rev. Sci. Instrum.* **2008**, *79*, 10E730. [[CrossRef](#)] [[PubMed](#)]
11. Scannell, R.; Walsh, M.J.; Dunstan, M.R.; Figueiredo, J.; Naylor, G.; O’Gorman, T.; Shibaev, S.; Gibson, K.J.; Wilson, H. A 130 point Nd:YAG Thomson scattering diagnostic on MAST. *Rev. Sci. Instrum.* **2010**, *81*, 10D520. [[CrossRef](#)] [[PubMed](#)]
12. Yamada, I.; Narihara, K.; Funaba, H.; Yasuhara, R.; Hayashi, H.; Kohmoto, T. Extension of the measurable temperature range of the LHD Thomson scattering system. *Rev. Sci. Instrum.* **2012**, *83*, 10E340. [[CrossRef](#)] [[PubMed](#)]
13. Knauer, J.P.; Pasch, E.; Kühner, G.; the W7-AS Team. High-resolution ruby laser Thomson scattering diagnostic for the W7-AS stellarator. *Rev. Sci. Instrum.* **2003**, *74*, 1679–1682. [[CrossRef](#)]
14. Giudicotti, L.; Pasqualotto, R.; Fassina, A. Dual-angle, self-calibrating Thomson scattering measurements in RFX-MOD. *Rev. Sci. Instrum.* **2014**, *85*, 11D823. [[CrossRef](#)] [[PubMed](#)]
15. Pan, W.; Wang, T.; Wang, Z.; Yang, Y.; Wu, H.; Verdoolaege, G.; Yang, Z.; Liu, C.; Guo, W.; Li, B.; et al. Integrated data analysis on the electron temperature profile of HL-2A with the Bayesian probability inference method. *Plasma Sci. Technol.* **2022**, *24*, 055601. [[CrossRef](#)]
16. Huang, Y.; Wang, Y.Q.; Hou, Z.P.; Ren, L.L.; Liu, C.H.; Feng, Z.; Luo, C.W. Multipoint vertical-Thomson scattering diagnostic on HL-2A tokamak. *Rev. Sci. Instrum.* **2018**, *89*, 10C116. [[CrossRef](#)] [[PubMed](#)]
17. Lee, J.H.; Lee, S.H.; Yamada, I. Design of practical alignment device in KSTAR Thomson diagnostic. *Rev. Sci. Instrum.* **2016**, *87*, 11E544. [[CrossRef](#)] [[PubMed](#)]
18. Sos, M.; Bohm, P.; Grover, O.; Bilkova, P.; Peterka, M.; Weinzettl, V.; Hron, M.; Panek, R. Observation and evaluation of the alignment of Thomson scattering systems. *Rev. Sci. Instrum.* **2018**, *89*, 10C105. [[CrossRef](#)] [[PubMed](#)]
19. Oh, S.; Lee, J.H. Collection optics design for KSTAR Thomson scattering system. *Rev. Sci. Instrum.* **2010**, *81*, 10D504. [[CrossRef](#)] [[PubMed](#)]

Disclaimer/Publisher’s Note: The statements, opinions and data contained in all publications are solely those of the individual author(s) and contributor(s) and not of MDPI and/or the editor(s). MDPI and/or the editor(s) disclaim responsibility for any injury to people or property resulting from any ideas, methods, instructions or products referred to in the content.